Cloud Resolving Modeling of the ARM Summer 1997 IOP: Model Formulation, Results, Uncertainties, and Sensitivities

MARAT F. KHAIROUTDINOV AND DAVID A. RANDALL

Department of Atmospheric Science, Colorado State University, Fort Collins, Colorado

(Manuscript received 1 October 2001, in final form 9 September 2002)

ABSTRACT

A new three-dimensional cloud resolving model (CRM) has been developed to study the statistical properties of cumulus convection. The model was applied to simulate a 28-day evolution of clouds over the Atmospheric Radiation Measurement Program (ARM) Southern Great Plains site during the summer 1997 Intensive Observation Period. The model was forced by the large-scale advective tendencies and surface fluxes derived from the observations. The sensitivity of the results to the domain dimensionality and size, horizontal grid resolution, and parameterization of microphysics has been tested. In addition, the sensitivity to perturbed initial conditions has also been tested using a 20-member ensemble of runs.

The model captures rather well the observed temporal evolution of the precipitable water and precipitation rate, although it severely underestimates the shaded cloud fraction possibly because of an inability to account for the lateral advection of clouds over the ARM site. The ensemble runs reveal that the uncertainty of the simulated precipitable water due to the fundamental uncertainty of the initial conditions can be as large as 25% of the mean values. Even though the precipitation rates averaged over the whole simulation period were virtually identical among the ensemble members, the timing uncertainty of the onset and reaching the precipitation maximum can be as long as one full day. Despite the predictability limitations, the mean simulation statistics are found to be almost insensitive to the uncertainty of the initial conditions.

The overall effects of the third spatial dimension are found to be minor for simulated mean fields and scalar fluxes but are quite considerable for velocity and scalar variances. Neither changes in a rather wide range of the domain size nor the horizontal grid resolution have any significant impact on the simulations. Although a rather strong sensitivity of the mean hydrometeor profiles and, consequently, cloud fraction to the microphysics parameters is found, the effects on the predicted mean temperature and humidity profiles are shown to be modest. It is found that the spread among the time series of the simulated cloud fraction, precipitable water, and surface precipitation rate due to changes in the microphysics parameters is within the uncertainty of the ensemble runs. This suggests that correlation of the CRM simulations to the observed long time series of the aforementioned parameters cannot be generally used to validate the microphysics scheme.

1. Introduction

Modeling of climate change requires clear understanding of feedbacks that operate in the climate system. Some of the most important yet uncertain feedbacks involve clouds. Because the individual clouds cannot be resolved by contemporary general circulation models (GCMs), their collective effects on the resolved large-scale flow has been parameterized using greatly simplified models of complex interactions among large-scale dynamics, clouds and radiation. Besides direct comparison of the climate simulated by GCMs to observations, parameterizations have been tested by running a GCM as a single-column model (SCM; Betts and Miller 1986), that is retaining all the physical processes operating in a GCM grid column, but prescribing the lateral advection of prognostic variables. Such advective tendencies can be derived from observations, then one can directly compare the evolution of simulated mean vertical profiles of various quantities to observations, which may help identify the problems with parameterizations in a given GCM.

A cloud resolving model (CRM) is a model capable of resolving most of the transport and heating associated with convective clouds for a simulated time period much longer than a life cycle of individual clouds. To control sinks and sources of momentum, mass, water, and energy during the course of a simulation, a domain with periodical lateral boundaries is usually applied. The main focus is on temporal and spatial statistics of an ensemble of clouds such as convective heating and moistening rates, convective mass flux, precipitation rates, etc., developing in response to specified external forcing. When CRMs are forced with the same large-scale tendencies as SCMs, they enable one to explicitly

Corresponding author address: Dr. Marat F. Khairoutdinov, Dept. of Atmospheric Science, Colorado State University, Fort Collins, CO 80523-1373.
E-mail: marat@atmos.colostate.edu

simulate the collective response of clouds to the applied external forcing in a ''column'' represented by a CRM domain (e.g., Xu and Randall 1996; Grabowski et al. 1998; Donner et al. 1999; Redelsperger et al. 2000; Tao et al. 2000; Xu et al. 2002). Detailed CRM output can then be used to supplement the observations for SCM evaluation (e.g., Gregory and Miller 1989; Randall et al. 1996; Ghan et al. 2000), or to promote new parameterization development (e.g., Randall et al. 1996). Recently, a CRM itself has been directly applied as a ''super parameterization'' of clouds in a realistic climate model (Khairoutdinov and Randall 2001). In the latter case, there is an explicit feedback of cloud-scale processes to large-scale flow.

It has become a standard practice to test the CRMs against high-quality observational datasets collected during intensive observation periods (IOPs) of such field programs as Global Atmospheric Research Program (GARP) Atlantic Tropical Experiment (GATE), Tropical Ocean and Global Atmosphere Coupled Ocean–Atmosphere Response Experiment (TOGA COARE), Atmospheric Radiation Measurement Program (ARM). However, even the highest quality observations cannot be as detailed as CRM output, so only a limited set of simulated statistics such as time series of the mean surface precipitation rate, shaded cloud fraction, surface bulk fluxes, and vertical profiles of temperature, water vapor and wind, are typically used for model validation. In addition, the observations themselves are not error-free, and the derived datasets may contain errors and inconsistencies even when sophisticated analysis techniques are applied (e.g., Zhang et al. 2001). However, from a cloud modeler's perspective, it is much more productive to address the uncertainties associated with the model itself, since any CRM contains parameterized physics of its own. The results may also be sensitive to the model domain size and geometry, grid resolution, and employed numerical methods.

Many CRM researchers have preferred two-dimensional (2D) CRMs over their three-dimensional (3D) counterparts, because multiday 2D simulations, even when one uses a domain as wide as a few thousand kilometers, are still relatively inexpensive, while computational cost of a comparable 3D simulation can be, in many cases, prohibitive. The important question has always been whether 2D CRMs are able to produce the cloud statistics similar to 3D CRMs (e.g., Tao and Soong 1986; Tao et al. 1987; Grabowski et al. 1998; Donner et al. 1999; Tompkins 2000; Petch and Gray 2001; Xu et al. 2002). Some studies concluded that, although one can always find some aspects of 2D simulations that differ rather significantly from 3D simulations, many important statistical characteristics, such as the mean temperature and water vapor profiles, cloud fraction, precipitation rates, mass fluxes, etc., tend to be similar, especially when 3D convection is two-dimensionally organized as, for example, in squall lines. However, in the case of clustered or random convection, it was found (Tompkins 2000) that 2D simulations can produce the thermodynamic sounding that can be substantially different from the one obtained in 3D simulations, especially in a low-surface-wind environment.

The desire to reduce computational cost has also motivated the choice of CRM domain size and resolution. It has become rather standard practice among CRM researchers to apply the horizontal grid resolution in the order of 1 or 2 km, arguing that such resolution still allows one to resolve the bulk of the vertical transport by deep clouds. For example, Xu and Randall (1995) found very little impact changing resolution from 2 to 1 km. Weisman et al. (1997) concluded that even 4-km resolution produces results comparable to 1-km resolution; this was also found by Khairoutdinov and Randall (2001). Grabowski et al. (1998) increased the resolution from 2 km to 200 m in their 2D simulations, and still reported no important effects, except for some decrease of cloud fraction and, consequently, changes of temperature in the upper troposphere, mostly because of changes in radiative cooling. However, Petch and Gray (2001) have noted a rather large impact on the convective updraft mass flux when resolution varied in the range from 500 m to 2 km. Bryan and Fritsch (2001) further argued that the spatial resolution in the order of 100 m is required for the subgrid-scale parameterizations of turbulence used by the CRMs to be valid. Sensitivity to the domain size has also received some attention (e.g., Xu and Randall 1995; Tompkins 2000; Petch and Gray 2001), with the general conclusion that as long as domain is large enough (typically larger than a few hundred kilometers) to accommodate the mesoscale organization of convective cells, the results are rather insensitive to the domain size.

The issue of sensitivity of CRM simulations to the domain geometry, size, and grid resolution is far from being settled; however, this issue should become less and less vital with dramatically reduced cost and increased computer power in the near future. There are, nonetheless, uncertainties associated with treatment of cloud microphysics and fundamental predictability limits imposed by nonlinearity of the equations that will not simply go away with increased computer power. Due to high computational demands of most CRM studies, there has been a tendency to use simpler ''bulk'' cloud microphysics schemes that would capture microphysical processes occurring during the life cycle of an individual cloud, but would use parameters that are ''tunable'' in a rather wide range. There have been relatively few studies of the effects of cloud microphysics scheme on the mean convective statistics as simulated by CRMs over the time periods as long as a few days (e.g., Grabowski 1998; Grabowski et al. 1999; Petch and Gray 2001). However, there have been, to our knowledge, no study of uncertainty of prolonged CRM simulations to initial conditions, although the use of so-called ensemble runs has become quite routine in the area of mesoscale, synoptic scale, and climate forecasting.

In this paper, we present a new three-dimensional parallel-processing CRM that has been developed at Colorado State University (CSU) to study the small- and mesoscale variability and organization of clouds and their effects on the environment. The model has been applied to simulate the evolution of clouds over the ARM Southern Great Plains (SGP) site using the large-scale and surface forcing data derived from the measurements obtained during 28 days of the ARM summer 1997 IOP. A major goal of this study was to test the sensitivity of simulations of strongly forced continental convection to domain dimensionality and size, horizontal grid resolution, and parameterization of microphysics. The sensitivity to the uncertainty of the initial conditions has also been tested using 20-member ensemble of 2D runs. To our knowledge, this is the first attempt to study the sensitivity of prolonged CRM runs to initial conditions. We will demonstrate that, in this case of strongly forced continental summertime convection, the uncertainty of time series of precipitation rate and precipitable water due to uncertainty of initial conditions, can be larger than the uncertainty associated with changes in the parameters that control the cloud microphysics scheme in the model.

The paper is organized as follows. Section 2 gives a brief description of the model equations and numerics and provides some details related to the design of numerical experiments. Section 3 discusses the results of the model sensitivity study. Section 4 offers a summary and conclusions.

2. Model description and simulation design

The dynamical framework of the model is based on the large eddy simulation (LES) model of Khairoutdinov and Kogan (1999). Besides using the anelastic equations of motion in place of the Boussinesq equations of the LES version, the new model uses a different set of prognostic thermodynamic variables and employs a different microphysics scheme. The computer code was also substantially modified to enable the model to run efficiently on parallel computers using the Message Passing Interface (MPI) protocol. The detailed description of the model equations is given in the appendix A.

The prognostic thermodynamical variables of the model are the liquid water/ice moist static energy, total nonprecipitating water (vapor + cloud water + cloud ice), and total precipitating water (rain + snow + graupel). The liquid water/ice moist static energy is, by definition, conserved during the moist adiabatic processes including the freezing/melting of precipitation. The cloud condensate (cloud water + cloud ice) is diagnosed using the so-called ''all-or-nothing'' approach, so that no supersaturation of water vapor is allowed. Despite being called a nonprecipitating water substance, the cloud ice is actually allowed to have a nonnegligible terminal velocity. It may be useful to note that the major difference between the precipitating ice (snow, hail, graupel) and cloud ice in the model is that the latter is assumed to be always in saturation with respect to water vapor, while the former can exist outside a cloud evaporating into an unsaturated environment. The partitioning of the diagnosed cloud condensate and the total precipitating water into the hydrometeor mixing ratios is done on every time step as a function of temperature. The diagnosed hydrometeor mixing ratios are then used to compute the water sedimentation and hydrometeor conversion rates.

The finite-difference representation of the model equations uses a fully staggered Arakawa C-type grid with stretched vertical and uniform horizontal grids. The advection of momentum is computed with the second-order finite differences in the flux form with kinetic energy conservation. The equations of motion are integrated using the third-order Adams–Bashforth scheme with a variable time step. All prognostic scalars are advected using a fully three-dimensional positive definite and monotonic scheme of Smolarkiewicz and Grabowski (1990). The subgrid-scale model employs the so-called 1.5-order closure based on a prognostic subgrid-scale turbulent kinetic energy, with an option to use a simple Smagorinsky-type scheme. The model uses periodic lateral boundaries, and a rigid lid at the top of the domain. To reduce gravity wave reflection and build-up, the Newtonian damping is applied to all prognostic variables in the upper third of the model domain. The surface fluxes are computed using Monin–Obukhov similarity.

The longwave and shortwave radiation scheme is adopted from the National Center for Atmospheric Research (NCAR) Community Climate Model (CCM3; Kiehl et al. 1998). The radiative transfer is computed for each individual grid column with the cloud radiative and optical properties explicitly calculated using the simulated cloud water and cloud ice mixing ratios. No effect of precipitating water on the cloud optical properties is currently considered. Due to the computational expense, radiation heating rates are updated every 3 min rather than every time step using the temperature, water vapor, and cloud water/ice fields averaged over the time interval between two calls to the radiation scheme following Xu and Randall (1995).

Figure 1 illustrates the large-scale forcing data used in this study. The data is taken from the objectively analyzed dataset (Zhang et al. 2001) derived from the observations made over the ARM SGP site in Oklahoma and Nebraska (36.5°N, 97.5°W) during the summer 1997 IOP from 2330 UTC 18 June (Julian day 170) to 2330 UTC 16 July (Julian Day 198). The dataset has been used for the CRM intercomparison study with this model, with participation among seven other CRMs as described by Xu et al. (2002). The observed horizontal and vertical large-scale advective tendencies for temperature and vapor mixing ratio are applied homogeneously at a given level and linearly interpolated in time from the 3 hourly data. To avoid uncertainties associated

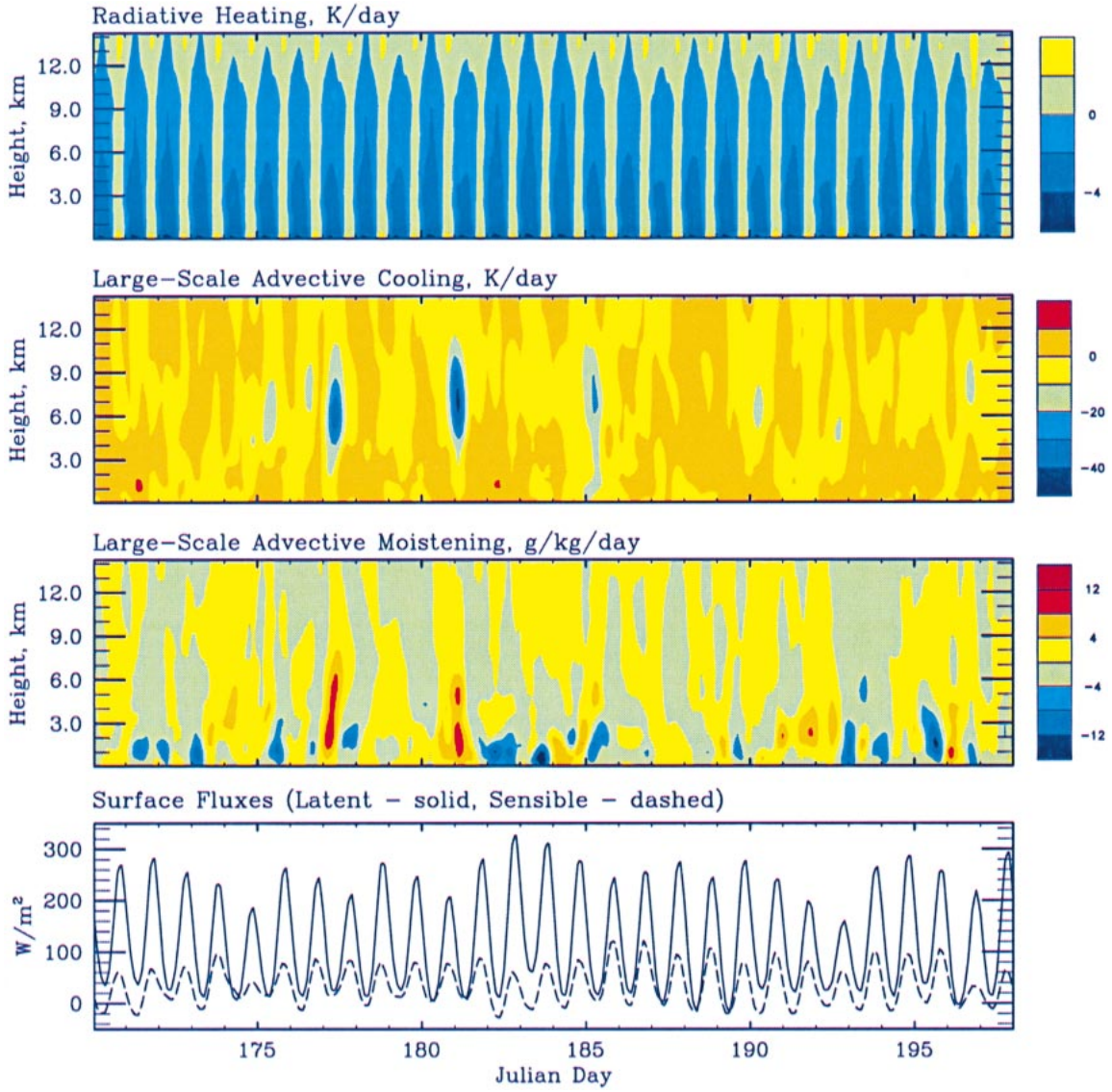

FIG. 1. (top to bottom) Time–height cross sections of the prescribed radiative cooling rates, large-scale advective cooling and moistening rates, and the surface latent and sensible heat fluxes.

with the treatment of land surface processes, the surface latent and sensible heat fluxes have been prescribed. The domain-averaged horizontal wind profile is nudged to the observed horizontal wind profile on a 2-h timescale. The radiative heating rate profile is imposed (except for the microphysics sensitivity runs) based on the profiles computed by the European Centre for Medium-Range Weather Forecasts (ECMWF) model, although the rates have been adjusted to preserve the column integral radiative heating derived from the variational analysis.

All runs use a 64-level vertical grid (capped at 27 km) with the first level at 50 m and grid spacing gradually increasing from 100 m near the surface to 500 m above 5 km. Most of the runs are 28 days long and use 2-km horizontal resolution and 10-s time step. The ensemble of runs has been generated using the identical model configuration and large-scale forcing, but a randomly perturbed initial thermodynamic sounding. As in the single-column model experiments of Hack and Pedretti (2000), perturbations with a standard deviation of 0.5 K for temperature and a maximum standard deviation of 0.5 g kg^{-1} for specific humidity in the boundary layer have been applied.

3. Results

a. 2D versus 3D runs and ensemble runs

Figure 2 compares to observations the time series of shaded cloud fraction, precipitable water, and precipi-

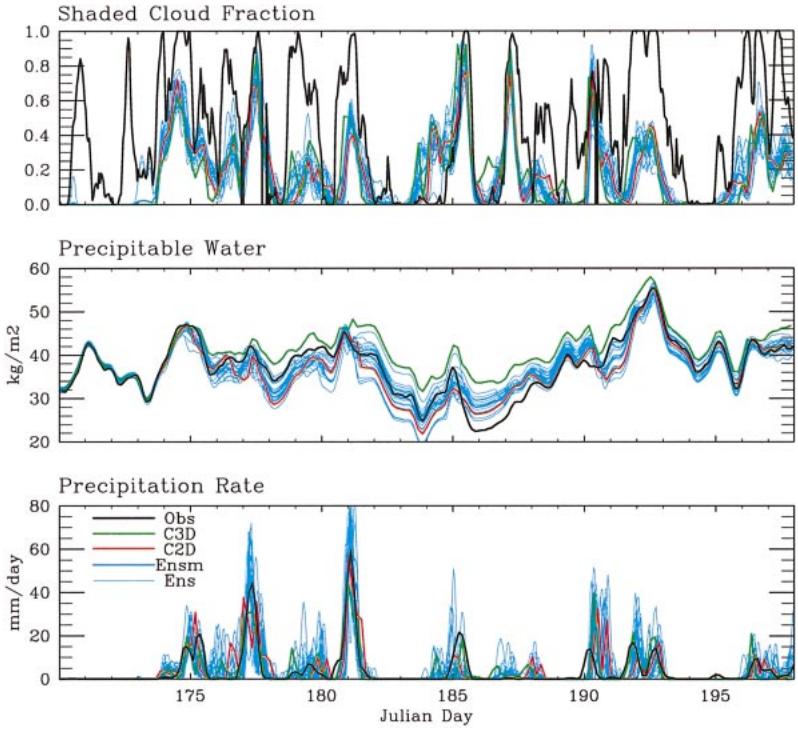

FIG. 2. Time series of simulated (top) shaded cloud fraction, (middle) precipitable water, and (bottom) surface precipitation rate for the control runs summarized in Table 1, and as observed. ''Ensm'' case represents the ensemble mean.

tation rate for both control runs and the ensemble runs with a corresponding ensemble mean. The runs are listed in Table 1. As one can see, the shaded cloud fraction defined as a fraction of all grid columns that have a cloud water/ice path exceeding 0.02 kg m^{-2}, is clearly underestimated with respect to the *GOES-7* satellite observations. Besides model deficiencies and the fact that the CRM with a 2-km horizontal resolution is generally not able to adequately resolve low-level boundary layer clouds, the lateral advection of high-level thin clouds into the space over the ARM site is most likely responsible for the underestimate. Overall, there is no clear difference between the cloud fraction predicted by the 2D and 3D models, both being within the uncertainty of the ensemble runs.

The observed temporal evolution of the precipitable water and surface precipitation are generally well captured by the 2D model. The 3D run tends to be considerably ''wetter.'' The ensemble mean precipitable water is generally close to the control run; however, the ensemble scatter can be as large as 12 kg m^{-2}, or about 25% of the mean. This happened, for example, after a solution bifurcation during Julian day 181. It is interesting to note that despite a rather wide spread among the precipitable water solutions, they tend to converge towards the end of the simulated period. A similar behavior of an ensemble, but in the context of a single-column model, was reported by Hack and Pedretti (2000). Even though the mean surface precipitation rate is virtually identical among all the runs, the timing of precipitation onset and reaching the maximum can vary rather widely. In fact, the precipitation onset uncertainty can be as long as one full day or even longer especially after prolonged dry periods.

Despite the fundamental uncertainty of the simulations due to nonlinearities of the model equations, the mean simulation statistics obtained by averaging over the whole 28-day period is rather robust and does not depend by any practical measure on the uncertainty of initial conditions as illustrated by Figs. 3 and 4. One can see that the ensemble envelope is generally narrow,

TABLE 1. Control runs.

Run	Domain	Size	Δt, *s*	Days	Comment
C3D	128 × 128 × 64	256 km × 256 km × 27 km	10	28	3D control
C2D	512 × 64	1024 km × 27 km	10	28	2D control
Ens	512 × 64	1024 km × 27 km	10	28	20-member ensemble runs

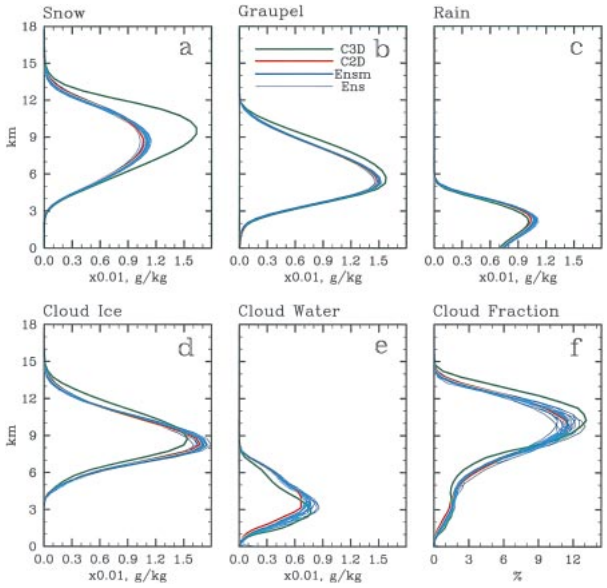

FIG. 3. Vertical profiles of (a) snow, (b) graupel, (c) rain, (d) cloud ice, and (e) cloud water mixing ratios; and (f) cloud fraction averaged over the entire time period of runs summarized in Table 1.

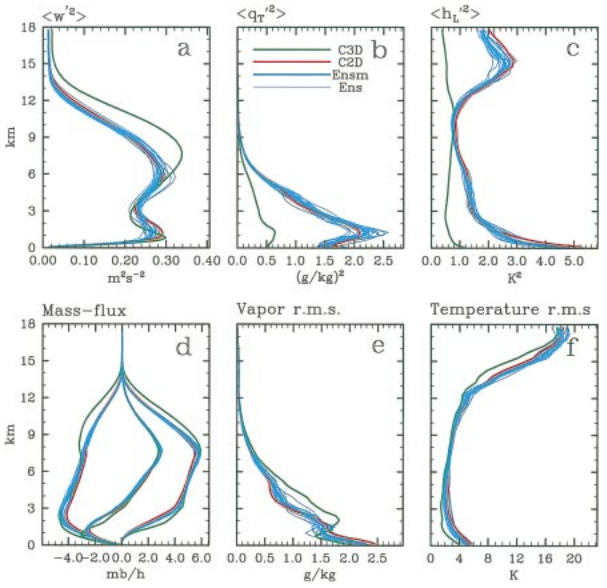

FIG. 4. Same as Fig. 3, but for (a) vertical velocity variance; (b) nonprecipitating water variance; (c) liquid/ice water moist static energy (divided by c_p) variance; (d) updraft (left curves), downdraft (right curves), and net (middle curves) mass fluxes; (e) water vapor rms error; and (f) temperature rms error with respect to observations.

which makes the apparent differences between the 2D and 3D results statistically significant.

There is rather little effect of the third spatial dimension on the vertical profiles of various hydrometeors (Figs. 3a–e) except for the slowly falling snow in the 3D run, which increases its content presumably due to additional suspension by stronger 3D updrafts. The 3D clouds seem to penetrate slightly deeper into the stable layer aloft as seen from the cloud fraction plot (Fig. 3f). Note that a grid point was assumed to be cloudy if the combined cloud water and cloud ice content exceeded 1% of the local saturation mixing ratio for water, similar to the procedure by Xu and Krueger (1991). The quantitative differences between the 2D and 3D cloud fraction profiles are relatively small, in fact comparable to the ensemble uncertainty range of the 2D runs. This supports earlier results of Grabowski et al. (1998) and Tompkins (2000) who showed little impact of the third spatial dimension on the cloud fraction in their tropical convection simulations.

The position and magnitude of the vertical velocity variance (Fig. 4a) in the 3D case differ rather significantly from those in 2D case suggesting stronger updrafts above the 5-km level. Even more dramatic differences can be seen in the variances of the total water (Fig. 4b) and liquid water/ice static energy (Fig. 4c). It is in agreement with earlier findings from the LES studies of convective boundary layers (e.g., Moeng et al. 1996) that 2D models of convection tend to agree well with 3D models on the evolution of mean fields and scalar fluxes, but may differ considerably in velocity and scalar variances due to fundamental differences between 3D and 2D turbulence. The variance maximum near the tropopause in Fig. 4c for the 2D case can be a result of breaking gravity waves, which, in the 2D case, do not decay with the distance from their source as fast as in the 3D case. Similar to the vertical velocity variance, the differences in the cloud updraft and downdraft mass fluxes (Fig. 4d) are only significant in the upper troposphere. However, the net cloud mass flux, constrained by the amount of the prescribed large-scale cooling, is virtually identical between the two cases despite the aforementioned differences in the strength of vertical motion. The profiles of scalar fluxes (not shown) are also found to be very similar. The root-mean-square (rms) errors with respect to observations of the water vapor (Fig. 4e) and temperature (Fig. 4f) have the maxima near the surface, about 2–2.5 g kg^{-1} and 4–6 K, respectively. The largest error in the temperature field is near the tropopause, most likely because of the errors in the prescribed radiative and advective tendencies.

Figure 5 shows the budgets of the nonprecipitating water (Fig. 5a), precipitating water (Fig. 5b), and all-water (Fig. 5c) for both cases averaged over the entire simulation period. Overall, the budgets for the 2D and 3D simulations are very similar with some subtle differences. One can see that the mean large-scale flow has a tendency to dry the boundary layer and moisten the low troposphere above it. Conversion of cloud water to precipitation is the main sink of the nonprecipitating water, which has two major sources in the troposphere (Fig. 5a). In the upper troposphere, it is the convergence of the total water flux due to deep convection, while in the lower troposphere, it is evaporation of the falling precipitation. It is remarkable that conversion of cloud

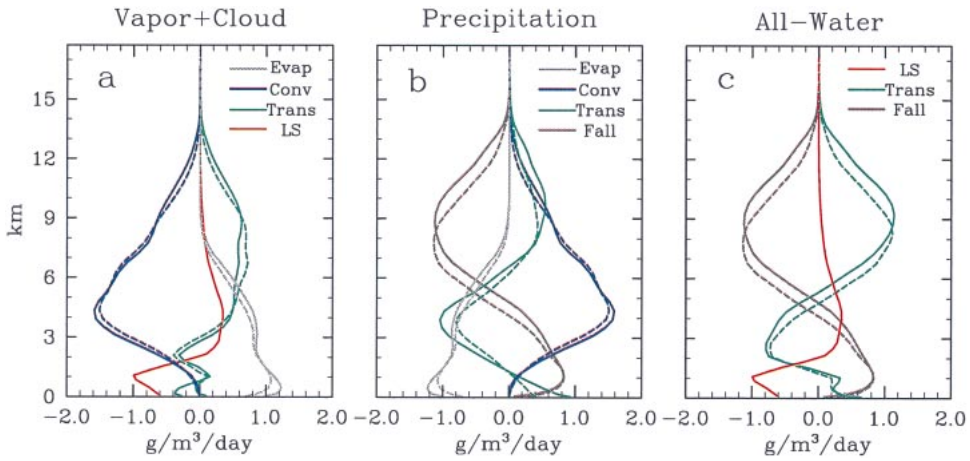

FIG. 5. The 28-day mean budgets of (a) nonprecipitating water, (b) precipitating water, and (c) all water as simulated by the 3D (solid lines) and 2D (dashed lines) CRM. Curves represent large-scale tendency (forcing) (LS); vertical (advection + diffusion) transport (Trans); conversion of cloud water into precipitation (Conv); tendency of precipitating water due to sedimentation (fallout) (Fall).

water is not a dominant source of precipitating water in the upper troposphere (Fig. 5b); rather, the transport of precipitation from the lower troposphere by the convective updrafts can be as important. The main sink of precipitating water in the upper troposphere is, of course, its fallout, but in the lower troposphere, it is evaporation into the environment. The all-water budget shows that in the upper troposphere there is an equilibrium between the vertical transport by the updrafts and removal by precipitation (Fig. 5c), while in the boundary layer, convergence of precipitation flux due to evaporation is a major term that counteracts the large-scale drying. This implies that evaporation of the falling precipitation is indeed a very important process that must be taken into account in convective parameterizations. Overall, the 3D case has a slightly higher evaporation rate, possibly due to higher mixing of the precipitating core with the environmental air, which is consistent with the wet bias in this case.

b. Sensitivity to horizontal resolution

In this study, due to relatively high cost of 3D runs, sensitivity to the horizontal grid resolution was tested using only the 2D CRM. The domain size was 1024 × 27 km and fixed with varying horizontal grid resolution Δx = 250 m, 500 m, 1 km, 2 km, 4 km, 8 km, 16 km, and 32 km (see Table 2). Note that the vertical grid was kept the same as in the control run. The time step also varied from Δt = 2 s to Δt = 10 s to satisfy the linear stability criterion.

One can see in Fig. 6 that resolution does not have any dramatic effect on microphysical profiles with the exception of cloud water, which shows progressively higher values as the resolution degrades. The cloud fraction (Fig. 6f) generally increases as the resolution decreases, which is consistent with Grabowski et al. (1998). As expected, the greatest sensitivity is exhibited by the vertical velocity variance (Fig. 7a), which is the measure of the strength of the resolved-by-grid vertical motions. The scalar variances (Figs. 7b and 7c), however, are not as sensitive as long as Δx stays below 16 km. This implies that most of the scalar field variance is mesoscale, which is still resolved by the coarse grid. Similar to vertical velocity, the updraft and downdraft mass fluxes (Fig. 7d) are quite sensitive to resolution in accord with the results of Petch and Gray (2001); however, the net mass flux is more robust. The same was found to be true for the mean profiles of various scalar fluxes (not shown). The rms errors (Figs. 7e and 7f) appear to be also insensitive to the grid resolution in the range considered in this study.

TABLE 2. Sensitivity to the horizontal grid resolution runs.

Run	Domain	Size	Δt, s	Days	Comment
G250	4096 × 64	1024 km × 27 km	2	28	Δx = 250 m
G500	2048 × 64	1024 km × 27 km	4	28	Δx = 500 m
G1000	1024 × 64	1024 km × 27 km	4	28	Δx = 1000 m
G4000	256 × 64	1024 km × 27 km	10	28	Δx = 4000 m
G8000	128 × 64	1024 km × 27 km	10	28	Δx = 8000 m
G16000	64 × 64	1024 km × 27 km	10	28	Δx = 16 000 m
G32000	32 × 64	1024 km × 27 km	10	28	Δx = 32 000 m

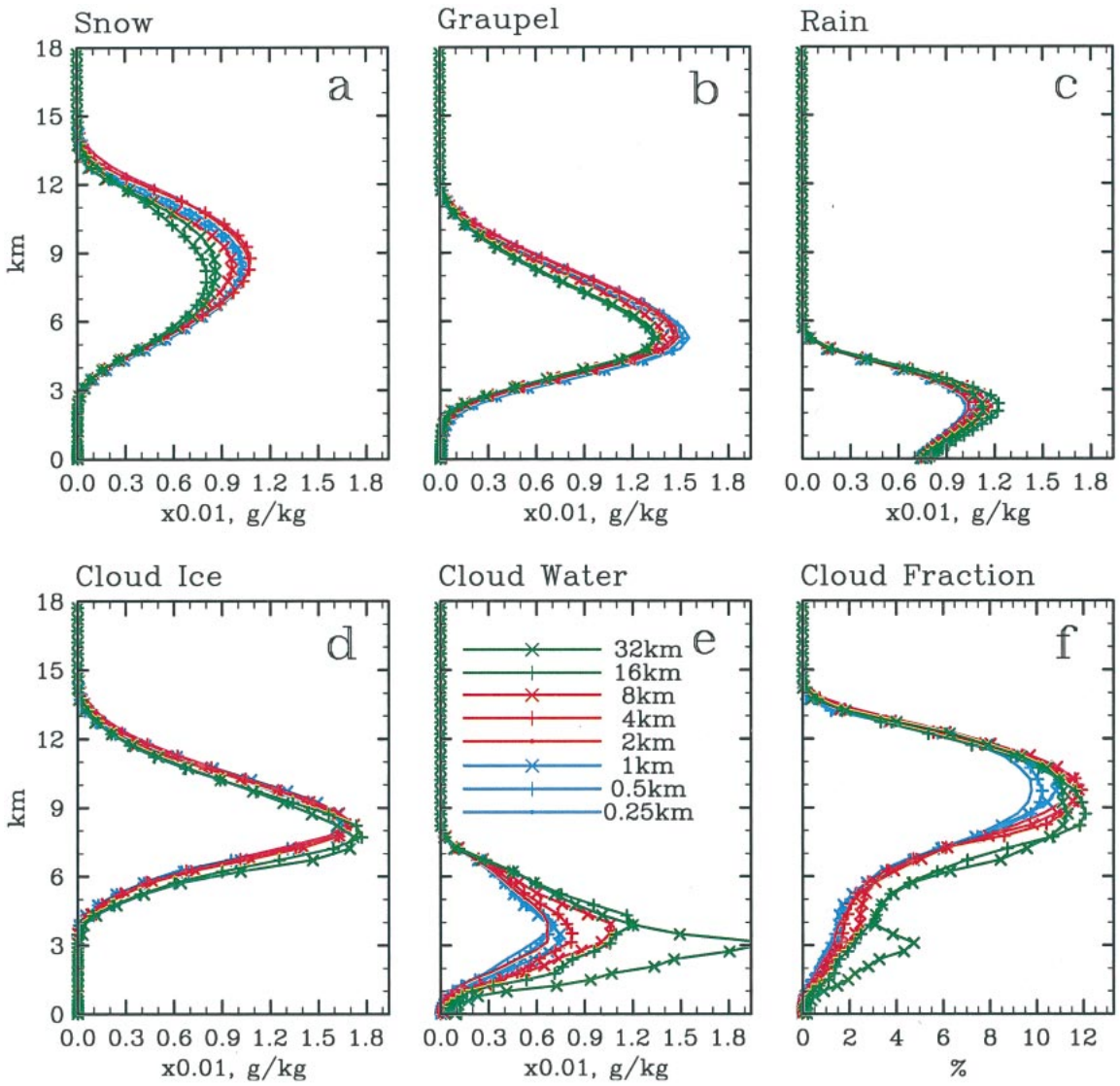

FIG. 6. Same as Fig. 3, but for the resolution sensitivity runs summarized in Table 2.

c. Sensitivity to the domain size

Sensitivity to the domain size was tested for both 2D and 3D versions of the model. To reduce the cost of 3D simulations, the runs were only 4 days long (see Table 3) and initialized using the observed sounding at 0000 UTC 27 July. The horizontal domain sizes varied from 256 km × 256 km to 1024 km × 1024 km for 3D runs, and from 512 to 9192 km for 2D runs. The horizontal grid resolution was 2 km. A complementary 20-member ensemble was also run using the 2D 512-km domain.

The simulated 4-day mean vertical profiles are shown in Figs. 8 and 9. One can see that there are apparent differences between the results corresponding to the 2D and 3D versions of the model, which are similar to those seen between the 28-day control runs. For a particular version of the model, there is very little sensitivity to the domain size, with the exception of horizontal velocity variance (Fig. 9c) and scalar variances (Figs. 9d and 9e). The latter tend to increase with the domain size as the result of mesoscale organization, since there is no sensitivity of the updraft intensity as indicated by the vertical velocity (Figs. 9a and 9b) and mass-flux statistics (Fig. 9f).

The time series in Fig. 10 shows rather small variability among the runs outside the range of the ensemble runs. Note that despite much shorter runs in this case and, therefore, higher expected predictability, strong bifurcation of the precipitable water still occurs right after a strong precipitation event during Julian day 181, similar to the control runs shown in Fig. 2. It is interesting that a similar range of variability is shown by eight different CRMs that simulated the same time period

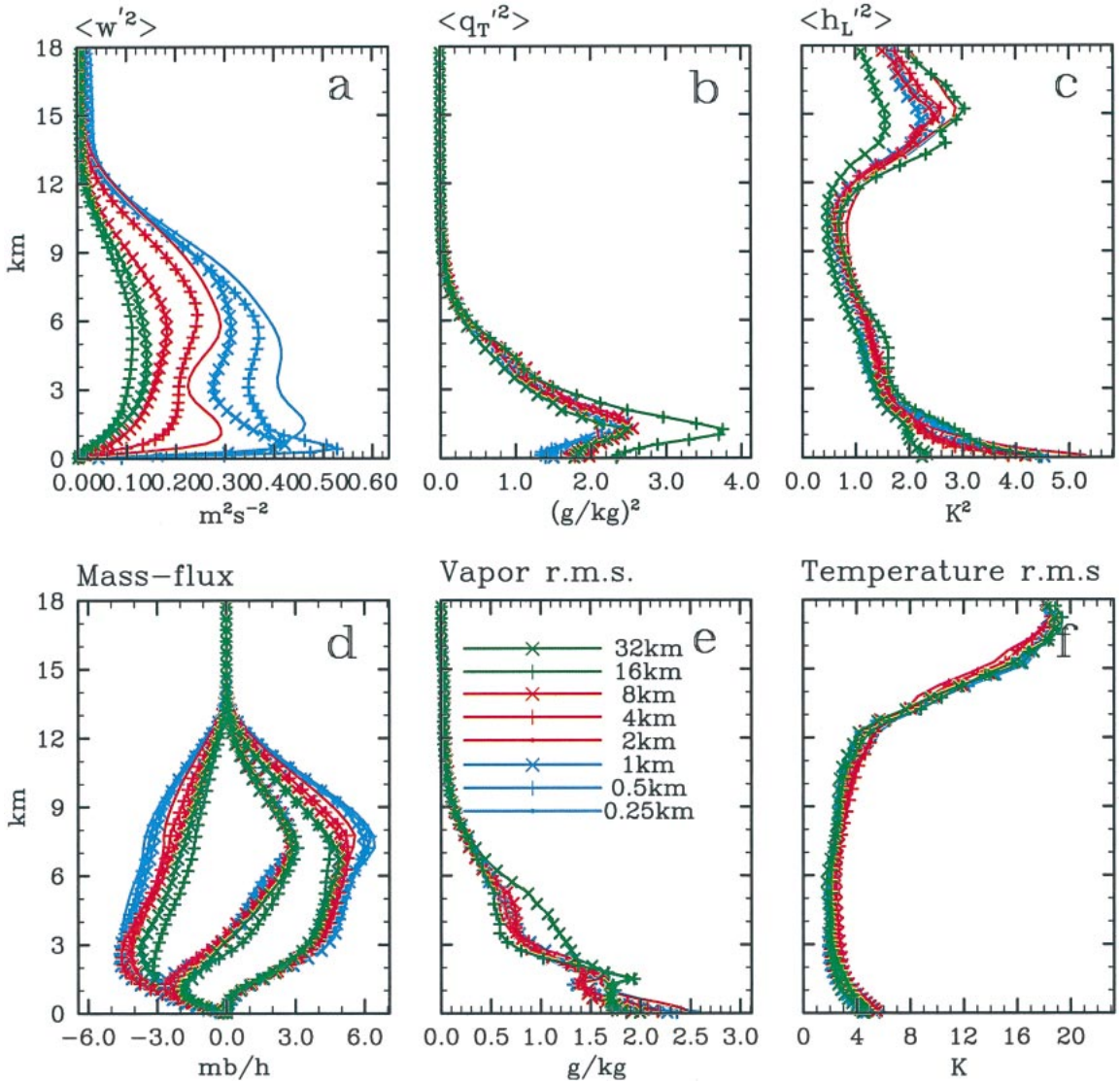

FIG. 7. Same as Fig. 4, but for the resolution sensitivity runs summarized in Table 2.

using the same forcing data, as presented by Xu et al. (2002; see their Fig. 3, subcase A).

d. Sensitivity to microphysics

Because of the feedbacks between the cloud microphysics and radiation, the sensitivity of the simulations to changes in the microphysics scheme was tested using interactive rather than prescribed radiation. All runs listed in Table 4 were done using the 2D CRM. In the control run, R512, the default set of microphysics parameters, given in the appendix B, was used. In the RLord run, the graupel and rain parameters were similar to those used by Lord et al. (1984), while in the RLin run, the graupel was replaced by hail with the properties similar to those used by Lin et al. (1983). In the RNoGr run, no graupel or hail was allowed altogether. The cloud ice sedimentation was switched off in the RNoIS run. The ice aggregation threshold was increased by a factor of 10 in the RQi3 run, and decreased by the same factor in the RQi5 run. Finally, the effects of autoconversion/aggregation rate coefficients were examined in runs RAutU and RAutD, where the coefficients were increased and decreased by one order of magnitude, respectively.

The 28-day mean vertical profiles of various quantities are shown in Figs. 11 and 12. As expected, the hydrometeor profiles are generally affected rather dramatically by the choice of microphysical parameters (Figs. 11a–e). The most significant change is in the snow amount when no graupel/hail is allowed (run RNoGr); one can see that the amount of slowly falling snow increases dramatically to maintain the precipitation flux constrained by the large-scale forcing. The changes to

TABLE 3. Sensitivity to domain size runs.

Run	Domain	Size	Δt, s	Days	Comment
A1283D	128 × 128 × 64	256 km × 256 km × 27 km	10	4	3D control
A2563D	256 × 256 × 64	512 km × 512 km × 27 km	10	4	Size ×2 over 3D control
A5123D	512 × 512 × 64	1024 km × 1024 km × 27 km	10	4	Size ×4 over 3D control
A256	256 × 64	512 km × 27 km	10	4	2D control
A512	512 × 64	1024 km × 27 km	10	4	Size ×2 over 2D control
A1024	1024 × 64	2048 km × 27 km	10	4	Size ×4 over 2D control
A2048	2048 × 64	4096 km × 27 km	10	4	Size ×8 over 2D control
A4096	4096 × 64	9192 km × 27 km	10	4	Size ×16 over 2D control
AE	256 × 64	512 km × 27 km	10	4	20-member ensemble runs

characteristics of graupel in the RLord and RLin runs also affect the mean snow and graupel profiles rather significantly. The mean cloud water and cloud ice are mostly sensitive to the autoconversion and ice aggregation rates (runs RAutU and RAutD) as well as to the threshold of ice aggregation (runs RQi3 and RQi5). Although setting the cloud ice sedimentation velocity to zero (run RNoIS) has almost no notable effect on the mean hydrometeor content, it strongly affects the cloud fraction (Fig. 11f) producing more extensive anvils

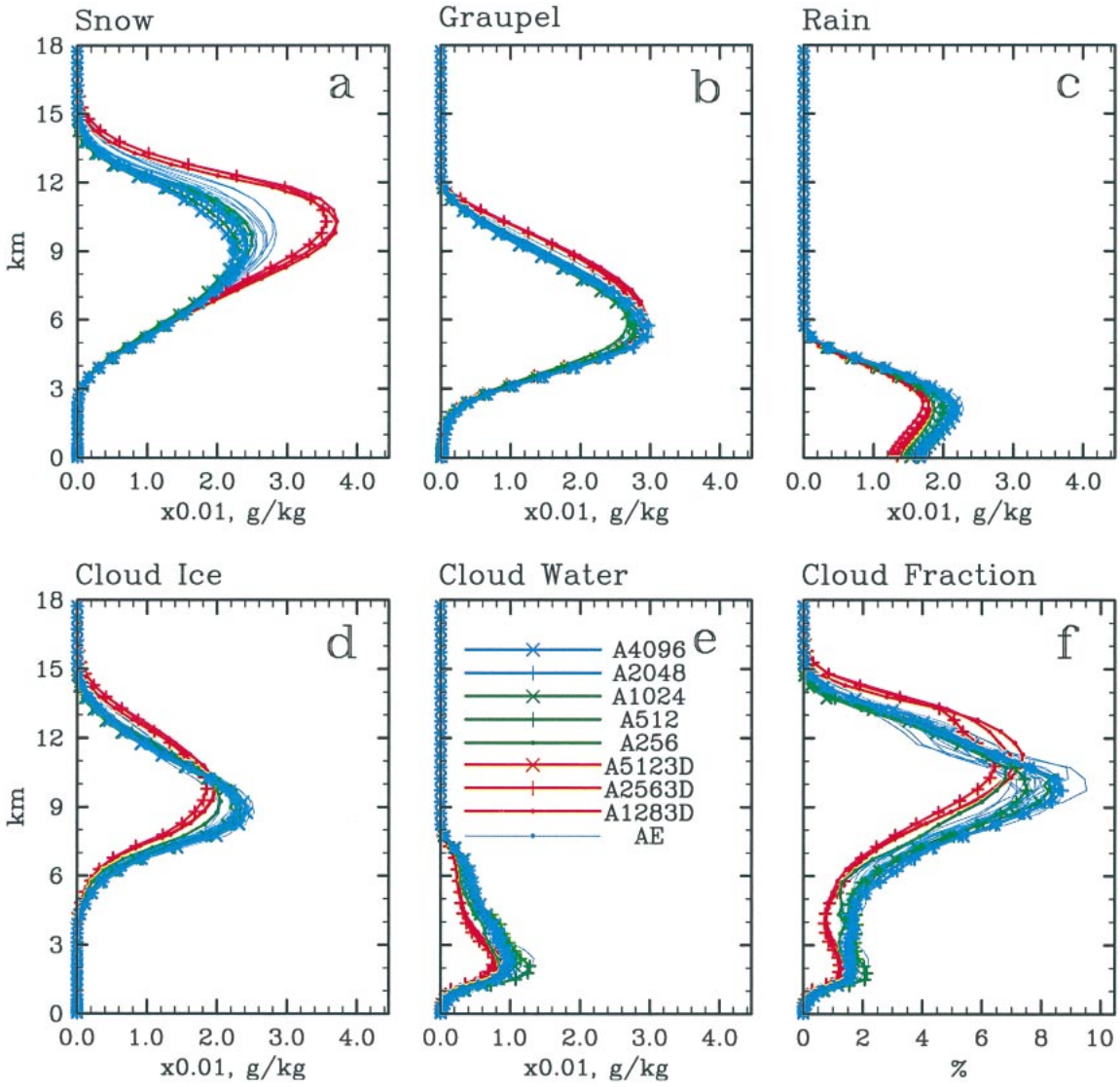

FIG. 8. Same as Fig. 3, but for the domain-size sensitivity runs summarized in Table 3.

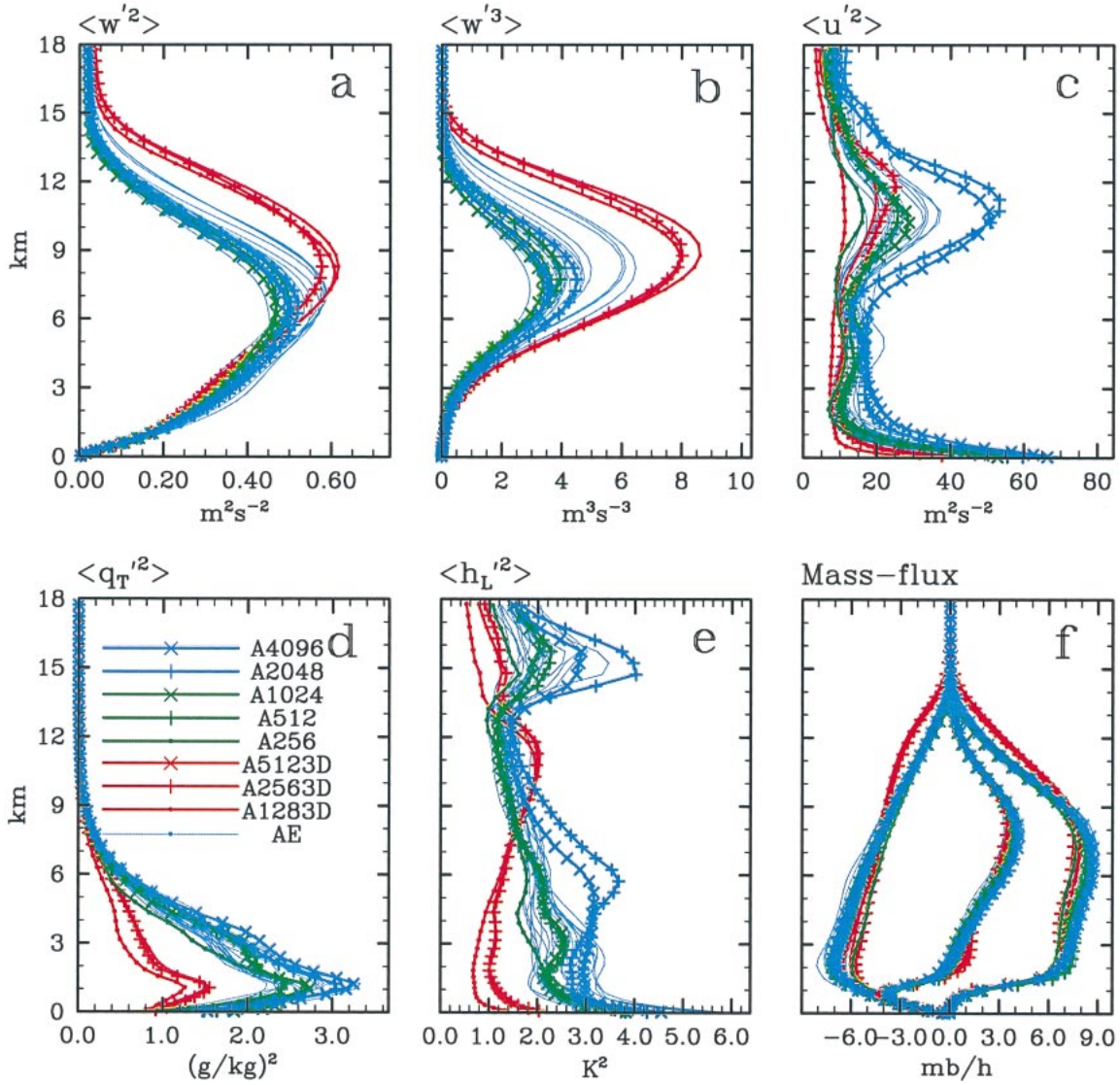

FIG. 9. Same as Fig. 8, but for (a) vertical velocity variance; (b) third moment of the vertical velocity; (c) horizontal velocity variance; (d) nonprecipitating water variance; (e) liquid/ice water moist static energy (divided by c_p) variance; and (f) updraft (left curves), downdraft (right curves), and net (middle curves) mass fluxes.

above 9 km. Overall, the simulated cloud fraction varies by a factor of two with monotonic dependence on the mean cloud ice content.

To maintain the precipitation flux profile, constrained by the large-scale cooling and, at the same time, maintain higher (lower) cloud water and cloud ice content in the RAutD and RQi3 (RAutU) runs, the convection must be more (less) vigorous than in the control run. This is demonstrated by the increased (decreased) updraft and downdraft mass flux profiles (Fig. 12a). Because the slowly falling snow tends to evaporate more over the same falling path than the quickly falling snow-graupel mixture, in the RNoGr run, more vigorous convection and thus, stronger updraft and downdraft mass fluxes are needed to maintain the mean precipitation. The net mass flux shows almost no sensitivity to changes in microphysics because of the quasiequilibrium of convection with the prescribed large-scale advective tendencies over a timescale of many days. As a result, the temperature (Fig. 12b) and water vapor (Fig. 12c) bias with respect to the control run are less then 1 K and 0.5 g m^{-3}, respectively.

The net radiative heating rate (Figs. 12d) changes most notably in the RAutD and RQi3 runs, as well as in the RNoIS run. In the former two runs, the net radiative cooling decreases below the cloud fraction maximum and increases above, while in the latter run, the net cooling tends to decrease rather uniformly throughout the anvil region. The plots of the longwave and shortwave components of the net radiative heating (Figs.

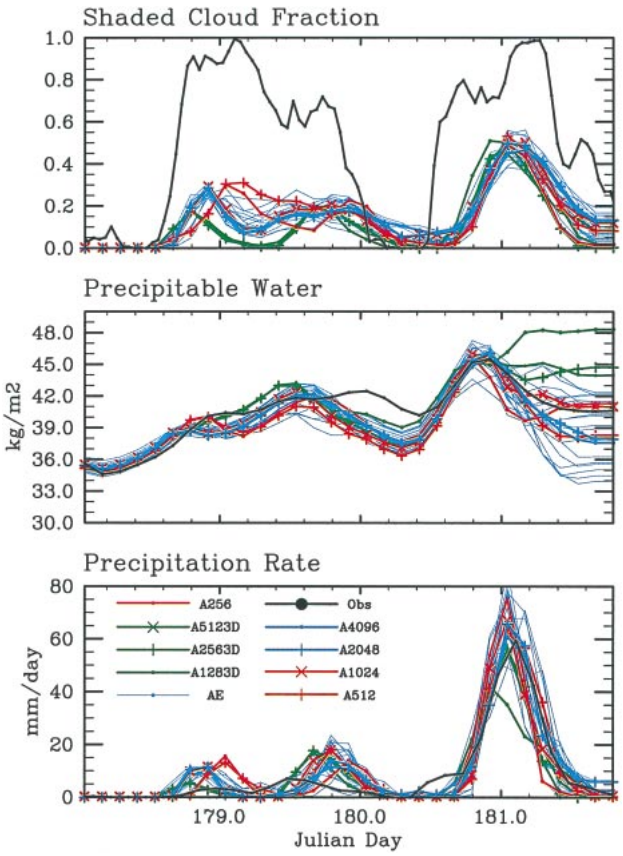

FIG. 10. Time series of simulated (top) shaded cloud fraction, (middle) precipitable water, and (bottom) surface precipitation rate for domain-size sensitivity runs summarized in Table 3, and as observed.

12e and 12f, respectively) show that the enhanced radiative cooling in the RAutD and RQi3 runs is mostly offset by the enhanced solar heating, while the additional trapping of the upwelling thermal radiation coming from the surface and the much warmer lower troposphere tends to reduce the clear sky cooling below 8 km. Similar effects are seen in the RNoIS run with the exception that the increase of the shortwave heating due to higher cloud area is not offset by the increased longwave cooling because of the lower ice content. Note that in the RAutU run, the impact of much higher autoconversion/aggregation rates on the radiative heating profile is opposite in sign to the impact of lower rates in the RAutD run.

Overall, the impact of changes in cloud microphysics scheme (within the limits of this study) on the mean statistics or climate of the simulations appears to be minor. This could be due to the fact that, in this particular case of strongly forced continental convection, the effects of cloud microphysics on simulated radiative heating and the characteristics of the hydrological cycle are mitigated by relatively low cloud occurrence frequency, and, more importantly, by the lack of feedbacks on the strong large-scale advective tendencies. Sensitivity to microphysics details could be amplified in the case of maritime tropical convection characterized by stronger cloud–radiation interactions and smaller effects of lateral advection.

It is interesting that despite rather dramatic changes made to the microphysics scheme, the results look reasonable in the sense that none of them can be definitely chosen as the preferred one since no detailed observations of the mean cloud statistics are available. One could suggest that perhaps the time series of such easily observed or retrieved macro characteristics as shaded cloud fraction, precipitable water, and precipitation rate, may be used to select the microphysical configuration that makes the CRM results correlate with observations most closely. However, the results shown in Fig. 13 suggest otherwise. Here, a time series uncertainty of an ensemble of runs is defined as a maximum spread among the members of that ensemble at various times. One can see that the uncertainty of the ensemble generated by changes to the microphysics parameters is mostly within the uncertainty of the 20-member ensemble generated by simply perturbing the initial sounding. Therefore, simple comparison to observations of simulated *long* time series of precipitable water or surface precipitation rate could not be generally used to verify bulk microphysics schemes, because the obtained sensitivity to microphysics may be within the noise generated by the nonlinearities of the model equations. We do not know how general this conclusion is, since only one particular case of continental convection is considered in this study, and more studies based on other cases are needed. It is rather curious that the results of much shorter 4-day simulations presented in the previous section (Fig.

TABLE 4. Sensitivity to microphysics runs.

Run	Domain	Size	Δt, s	Days	Comment
R512	512 × 64	1024 km × 27 km	10	28	2D control with interactive radiation
RLord	512 × 64	1024 km × 27 km	10	28	$\rho_g = 300$ kg m^{-3}, $N_{og} = 4 \times 10^4$ m^{-4}, $N_{or} = 22 \times 10^6$ m^{-4} (Lord et al. 1984)
RLin	512 × 64	1024 km × 27 km	10	28	$\rho_g = 917$ kg m^{-3}, $N_{og} = 4 \times 10^4$ m^{-4} (Lin et al. 1983)
RNoGr	512 × 64	1024 km × 27 km	10	28	No graupel/hail
RNoIS	512 × 64	1024 km × 27 km	10	28	No cloud ice sedimentation
RQi3	512 × 64	1024 km × 27 km	10	28	$q_{i0} = 10^{-3}$ kg kg^{-1}
RQi5	512 × 64	1024 km × 27 km	10	28	$q_{i0} = 10^{-5}$ kg kg^{-1}
RAutU	512 × 64	1024 km × 27 km	10	28	$\alpha = \beta = 0.01$ s^{-1}
RAutD	512 × 64	1024 km × 27 km	10	28	$\alpha = \beta = 0.0001$ s^{-1}

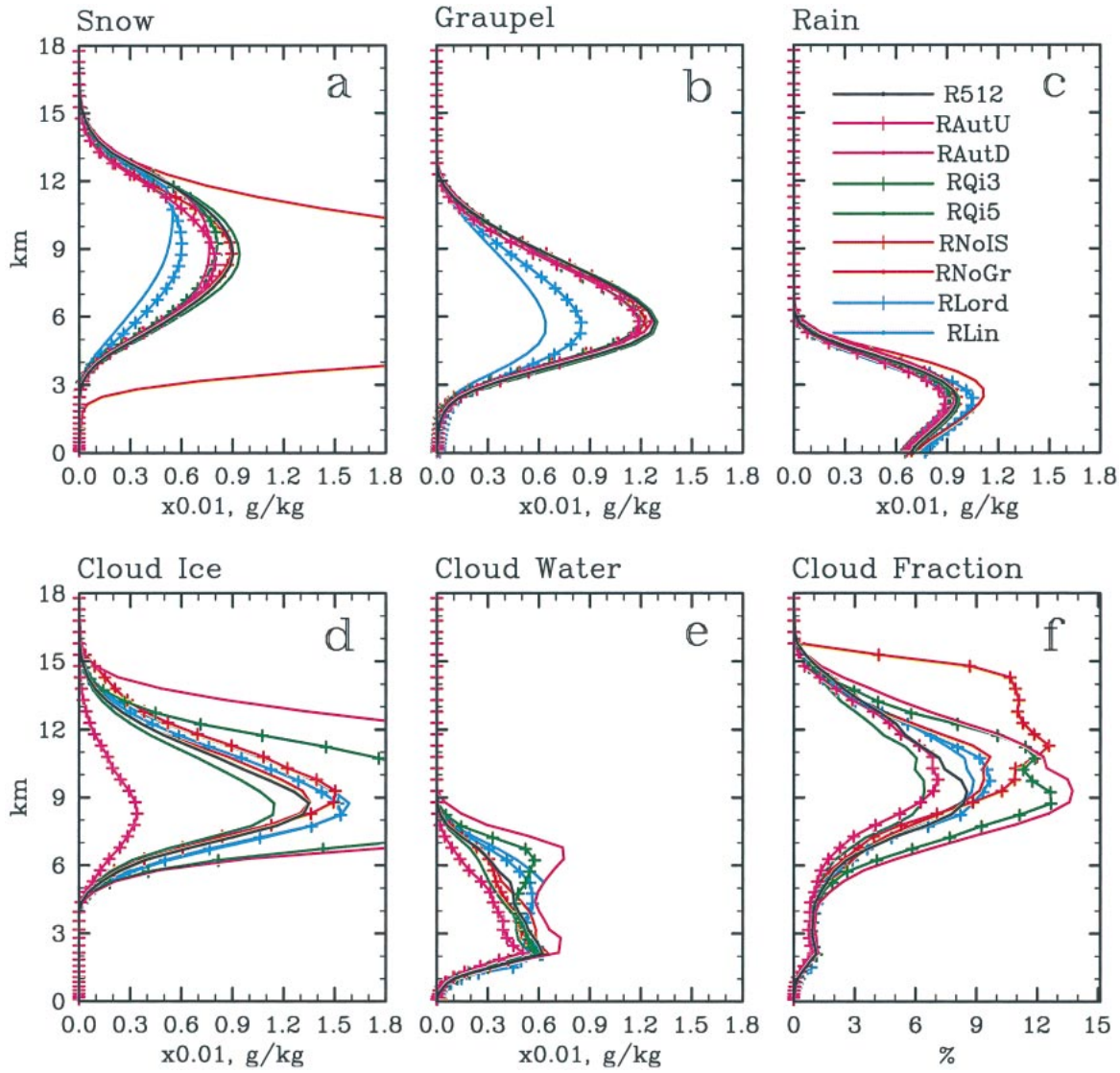

FIG. 11. Same as Fig. 3, but for microphysics sensitivity runs summarized in Table 4.

10) also show strong bifurcation of the solution on a timescale shorter than 1 day, suggesting that perhaps predictability of relatively short (a few days) cloud ensemble simulations may also be rather questionable.

4. Summary and conclusions

A new three-dimensional CRM has been developed at Colorado State University to study the small- and mesoscale variability and organization of clouds and their effects on the environment. The parallel computing technology based on Message Passing Interface (MPI) protocol allows the use of large spatial domains to study idealized interactions of clouds with the large-scale circulation.

In this study, the model has been applied to simulate the evolution of clouds over the ARM SGP site using the large-scale and surface forcing data derived from the measurements obtained during 28 days of the ARM summer 1997 IOP. A major goal was to test the sensitivity of the results to domain dimensionality and size, horizontal grid resolution, parameterization of microphysics, and the uncertainty of the initial conditions.

The effects of the third spatial dimension are found to produce more intense vertical motions especially in the anvil regions of the simulated clouds; however, virtually no differences are found in the vertical distribution of hydrometeors with the exception of slowly falling snow apparently due to suspension by stronger 3D updrafts. In accord with earlier LES studies of the stratocumulus-topped boundary layers (e.g., Moeng et al. 1996), the 2D CRM results tend to agree well with the 3D CRM results on the evolution of mean fields and scalar fluxes, but differ quite considerably in velocity and scalar variances.

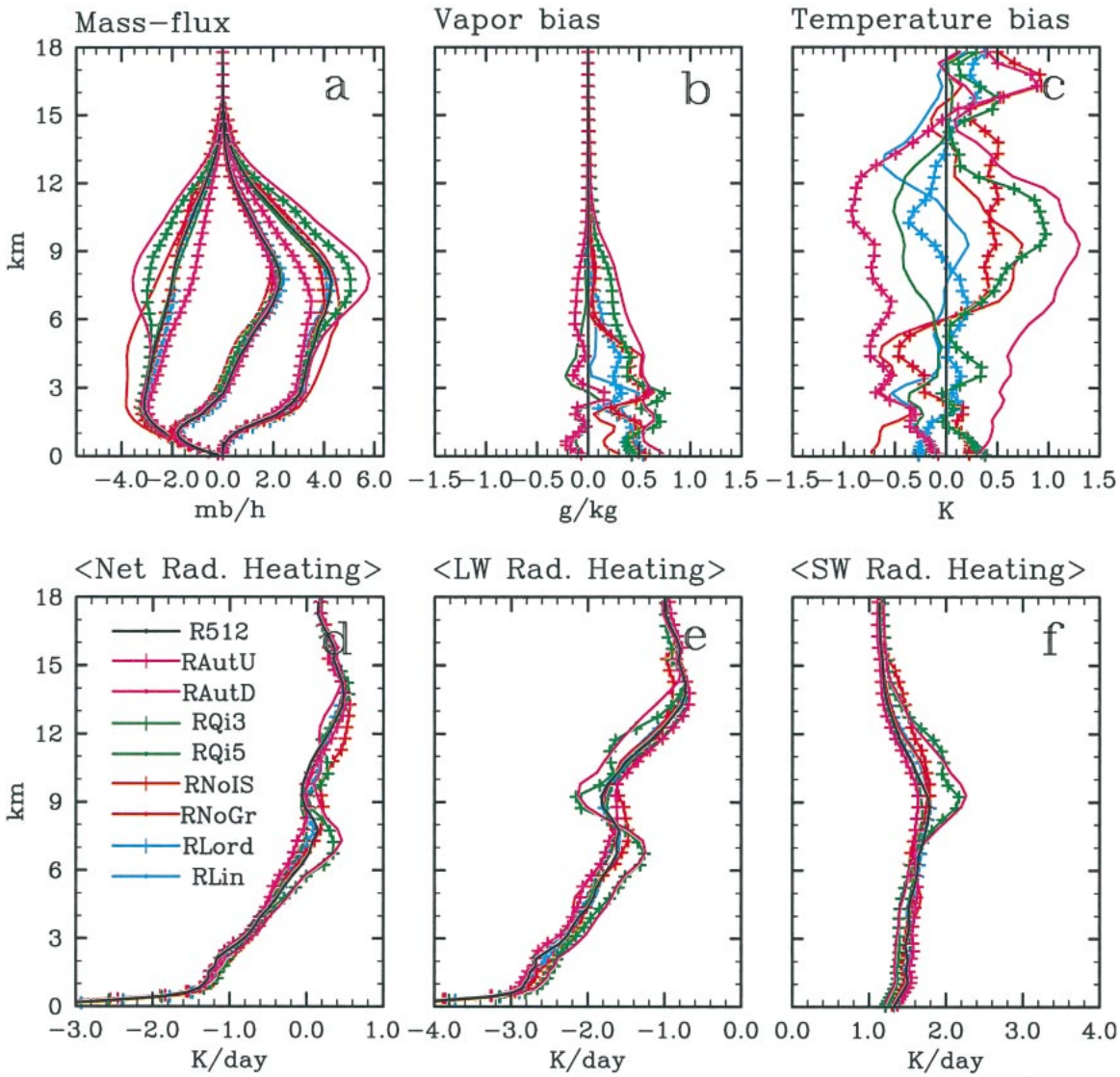

FIG. 12. Same as Fig. 11, but for (a) updraft (left curves), downdraft (right curves), and net (middle curves) mass fluxes; (b) water vapor bias and (c) temperature bias, with respect to the control R512 run; and (d) net, (e) longwave, and (f) shortwave radiative heating rates.

The time series of simulated shaded cloud fraction, precipitable water, and precipitation rate have been directly compared to observations. It is found that shaded cloud fraction is significantly underestimated with respect to the *GOES-7* satellite observations, most likely due to the lateral advection of high clouds over the ARM site that we could not account for in the model. The observed temporal evolution of the precipitable water and surface precipitation rate are captured rather well, although the 3D CRM tends to be somewhat wetter. The ensemble runs demonstrate that uncertainty of simulated precipitable water can be as large as 25% of the mean values. The ensemble runs also demonstrate that there is a predictability limit of at least 1 day on how well the model is able to reproduce the timing of the precipitation onset and maximum, as well as its amplitude. However, the statistics obtained by averaging the results over the whole 28-day period shows virtually no sensitivity to the uncertainty of the initial conditions.

The sensitivity to horizontal grid resolution has been tested over a rather wide range, from 250 m to 32 km, using the 2D CRM and fixed domain size. Not surprisingly, the resolved-by-grid quantities such as the vertical velocity variance, or updraft and downdraft mass fluxes are found to be quite sensitive to the grid resolution; however, the net cloud mass flux does not show notable sensitivity, apparently being strongly constrained by the prescribed large-scale forcing. The hydrometeor mixing ratio and cloud fraction profiles also show virtually no sensitivity as long as the grid resolution is finer than 4

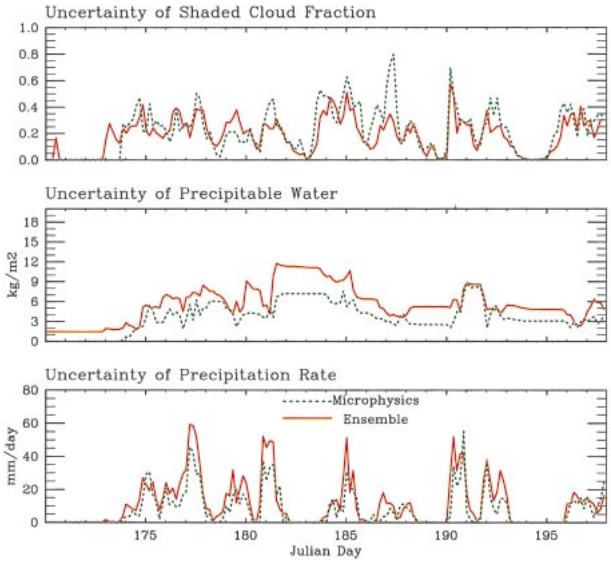

FIG. 13. (top to bottom) Uncertainty of the time series of the simulated shaded cloud fraction, precipitable water, and surface precipitation rate for the ensemble runs (solid lines) and the sensitivity-to-microphysics runs (dashed lines). The uncertainty is defined as a maximum spread among the runs at various times.

km. A relatively good performance of the model with such coarse horizontal resolution as 16 km and even 32 km was very surprising suggesting that, perhaps, strongly forced CRM simulations could be too self-constrained and may not fully reveal the model deficiencies.

Sensitivity to the domain size has been tested for both 2D and 3D CRMs using much shorter 4-day simulations to accommodate the computationally expensive 3D simulations performed over the domain as small as 256 km $\times$ 256 km, and as large as 1024 km $\times$ 1024 km. The 2D simulations were performed for even wider domains ranging from 512 to 9192 km. Besides the familiar differences between the 2D and 3D models, we found very little sensitivity to the size of the domain of the same dimensionality. Despite much higher expected predictability of the 4-day runs compared to the 28-day runs, a strong bifurcation of the precipitable water after a strong precipitation event was found to be similar to the one that occurred in much longer runs.

Sensitivity to the parameters that prescribe characteristics of the precipitating hydrometeors, water autoconversion and ice aggregation rates, cloud ice aggregation threshold, and cloud ice sedimentation velocity, was also tested using interactive radiation rather than prescribed rates. As expected, the hydrometeors mixing ratios are strongly affected by the changes to the microphysics scheme as is the simulated cloud fraction, with the latter varying within a factor of two. It is found that changes to the autoconversion/accretion rate coefficients, as well as the increase of the cloud ice aggregation threshold, affect the amount of cloud water and ice most profoundly, and have the strongest effects on the mean dynamical and thermodynamical statistical properties of the simulated convection. However, the effects on the predicted mean temperature and moisture bias are found to be relatively modest, most likely, due to relatively low cloud occurrence frequency and rather strong large-scale advective tendencies in this particular case of continental convection.

It is also found that the spread among the time series of the simulated shaded cloud fraction, precipitable water, and precipitation rates for different configurations of the microphysics scheme is mostly within the range of the ensemble runs. This rather unexpected result strongly suggests that long time series, like the ones used in this study, may be, in general, inadequate to verify the accuracy of microphysics schemes because it might be difficult to differentiate the changes that occurred due to a particular modification to the microphysics scheme from those that occurred simply by chance. Therefore, it may be useful to estimate the fundamental uncertainty of CRM simulations using ensemble runs *before* making any definitive conclusions about the sensitivity of CRM simulations to various model parameters, because some of the revealed sensitivities could in fact be statistically insignificant.

In conclusion we would like to stress that this study was not intended to reveal the full range of the model physical sensitivities and uncertainies because of the restrictive nature of prescribed external forcing with no feedbacks. Such sensitivities could be amplified when such feedbacks to the large-scale circulation are included, a subject that we may explore in the future.

Acknowledgments. This research was supported in part by the U.S. Department of Energy Grant DE-FG03-02ER63323 to Colorado State University as part of the Atmospheric Radiation Measurement Program, and National Science Foundation Grant ATM-9812384 to Colorado State University.

APPENDIX A

Model Equations

a. Prognostic equations

The anelastic momentum and scalar conservation and continuity equations are written in tensor notation as

$$\frac{\partial u_i}{\partial t} = -\frac{1}{\overline{\rho}}\frac{\partial}{\partial x_j}(\overline{\rho} u_i u_j + \tau_{ij}) - \frac{\partial}{\partial x_i}\frac{p'}{\overline{\rho}} + \delta_{i3} B + \varepsilon_{ij3} f (u_j - U_{gj}) + \left(\frac{\partial u_i}{\partial t}\right)_{\text{l.s.}}, \tag{A1}$$

$$\frac{\partial}{\partial x_i}\overline{\rho} u_i = 0, \tag{A2}$$

$$\frac{\partial h_L}{\partial t} = -\frac{1}{\overline{\rho}}\frac{\partial}{\partial x_i}(\overline{\rho}u_i h_L + F_{h_L i}) - \frac{1}{\overline{\rho}}\frac{\partial}{\partial z}(L_c P_r + L_s P_s + L_s P_g) + \left(\frac{\partial h_L}{\partial t}\right)_{\text{rad}} + \left(\frac{\partial h_L}{\partial t}\right)_{\text{l.s.}}, \quad \text{(A3)}$$

$$\frac{\partial q_T}{\partial t} = -\frac{1}{\overline{\rho}}\frac{\partial}{\partial x_i}(\overline{\rho}u_i q_T + F_{q_T i}) - \left(\frac{\partial q_p}{\partial t}\right)_{\text{mic}} + \left(\frac{\partial q_T}{\partial t}\right)_{\text{l.s.}}, \quad \text{and} \quad \text{(A4)}$$

$$\frac{\partial q_p}{\partial t} = -\frac{1}{\overline{\rho}}\frac{\partial}{\partial x_i}(\overline{\rho}u_i q_p + F_{q_p i}) + \frac{1}{\overline{\rho}}\frac{\partial}{\partial z}(P_r + P_s + P_g) + \left(\frac{\partial q_p}{\partial t}\right)_{\text{mic}}. \quad \text{(A5)}$$

Here, $u_i (i = 1, 2, 3)$ are the resolved wind components along the Cartesian x, y, and vertical z directions, respectively; ρ is the air density; p is pressure; h_L is liquid/ice water static energy $[= c_p T + gz - L_c(q_c + q_r) - L_s(q_i + q_s + q_g)]$; q_T is total nonprecipitating water (water vapor + cloud water + cloud ice) mixing ratio $(= q_v + q_c + q_i = q_v + q_n)$; q_p is total precipitating water (rain + snow + graupel) mixing ratio $(= q_r + q_s + q_g)$; f is Coriolis parameter; U_g is prescribed geo strophic wind; B is buoyancy $[= -g(\rho'/\rho) \approx g(T'/\overline{T} + 0.608\, q_v' - q_n - q_p - p'/\overline{p})]$; g is gravitational acceleration; c_p is specific heat at constant pressure; L_c and L_s are latent heat of evaporation and sublimation, respectively; $\boldsymbol{\tau}_{ij}$ is subgrid-scale stress tensor; F_{h_L}, F_{q_T}, and F_{q_p} are subgrid-scale scalar fluxes; P_r, P_s, and P_g are rain, snow, and graupel precipitation fluxes, respectively; the subscript ''rad'' denotes the tendency due to radiative heating; ''mic'' represents the tendency of precipitating water due to conversion of cloud water/ice and due to evaporation; ''l.s.'' denotes the prescribed large-scale tendency; the overbar and prime represent the horizontal mean and perturbation from that mean, respectively.

b. Subgrid-scale (SGS) model

The SGS model has been adopted from the LES model of Khairoutdinov and Kogan (1999), and is similar to the 1.5-order closure model of Deardorff (1980). The model has also an option to use a simple first-order Smagorinsky closure scheme. Both closures define the local moist Brunt–Väisälä frequency in terms of the model thermodynamic variables as

$$N^2 = \left(\frac{g}{\overline{T}}\right)\frac{\partial}{\partial z}\frac{[h_L + 0.61 T c_p q_T + (L - c_p T)q_p]}{c_p} \quad \text{outside cloud, and} \quad \text{(A6)}$$

$$N^2 = \left(\frac{g}{\overline{T}}\right)\frac{\partial}{\partial z}\left[\frac{h_L + (L - c_p T)(q_T + q_p)}{c_p + L(\partial q_s/\partial T)}\right] \quad \text{inside cloud.} \quad \text{(A7)}$$

The SGS eddy exchange coefficient is proportional to the local grid scale squared, which is usually computed in LES models as a geometric mean of all three grid spacings. However, in cloud resolving simulations of deep convection, it is rather typical (especially near the surface) for the horizontal grid to be much coarser than the vertical grid, which can lead to high values of the SGS eddy exchange coefficient, and thus, to artificially excessive vertical mixing. To prevent this undesirable behavior, only the vertical grid spacing is used as the SGS grid length scale in the case of highly anisotropic grids.

c. Hydrometeor partitioning

The partitioning among the hydrometeors is assumed to be as follows:

$$q_c = \omega_n q_n, \quad \text{(A8)}$$

$$q_i = (1 - \omega_n)q_n, \quad \text{(A9)}$$

$$q_r = \omega_p q_p, \quad \text{(A10)}$$

$$q_s = (1 - \omega_p)(1 - \omega_g)q_p, \quad \text{and} \quad \text{(A11)}$$

$$q_g = (1 - \omega_p)\omega_g q_p, \quad \text{(A12)}$$

where the partition functions ω_n, ω_p, and ω_g depend only on temperature:

$$\omega_m = \max\left[0, \min\left(1, \frac{T - T_{00m}}{T_{0m} - T_{00m}}\right)\right], \quad \text{(A13)}$$

where, $m = n, p, g$,

so that $\omega_m = 0$ for $T \le T_{00m}$, $\omega_m = 1$ for $T \ge T_{0m}$, and $0 < \omega_m < 1$ for $T_{00m} < T < T_{0m}$.

The total cloud condensate (cloud water + cloud ice) q_n is diagnosed from the prognostic thermodynamical variables along assuming the so-called all-or-nothing approach, so that no excess of water vapor with respect to the water vapor saturation mixing ratio is allowed. The latter is defined as a linear combination of the saturation mixing ratios over water and ice:

$$q_{\text{sat}} = \omega_n q_{\text{satw}} + (1 - \omega_n)q_{\text{sati}}. \quad \text{(A14)}$$

Given the liquid/ice water static energy h_L, total nonprecipitating q_T and total precipitating q_p water mixing ratios, and adopting the partitioning relations (A8)–(A14), one can diagnose the temperature and, consequently, the mixing ratio of various hydrometeors using a suitable iterative procedure. In this model, we use a variant of the rapidly converging Newton–Raphson iterative method.

d. Bulk microphysics equations

The conversion rates among the hydrometeors are parameterized assuming that a number concentration N_m

of any precipitating water type m is distributed with hydrometeor size D_m according to Marshall and Palmer (1948):

$$\frac{\partial N_m}{\partial D} = n_m(D_m) = N_{0m} \exp(-\lambda_m D_m), \quad \text{(A15)}$$

where N_{0m} is the so-called intercept parameter, and

$$\lambda_m = \left(\frac{\pi \rho_m N_{0m}}{q_m \rho}\right)^{1/4}. \quad \text{(A16)}$$

If we assume that the hydrometeor particle terminal velocity can be expressed as

$$v_m(D_m, p) = a_m D_m^{b_m} \left(\frac{\rho_o}{\rho}\right)^{0.5}, \quad \text{(A17)}$$

then precipitation flux due to precipitating water type m, defined as

$$P_m(p) = \rho q_m V(p) = \rho q_m \left\{ \left[\int_0^\infty n_m(D_m) v_m(D_m, p) D_m^3 \, dD_m \right] \div \left[\int_0^\infty n_m(D_m) D_m^3 \, dD_m \right] \right\}, \quad \text{(A18)}$$

can be written using (A15)–(A17) as

$$P_m(p) = \frac{a_m \Gamma(4 + b_m)}{6} (\pi \rho_m N_{0m})^{-b_m/4} \left(\frac{\rho_o}{\rho}\right)^{0.5} (\rho q_m)^{1 + b_m/4}. \quad \text{(A19)}$$

The rate of change of mixing ratio of precipitating type m due to the mass change of individual hydrometeor particles of mass M_m is written in general form as

$$\frac{\partial q_m}{\partial t} = \rho^{-1} \int_0^\infty \frac{\partial M_m}{\partial t} n(D_m) \, dD_m. \quad \text{(A20)}$$

In case of precipitation evaporation,

$$\left(\frac{\partial M_m}{\partial t}\right)_{\text{evap}} = \frac{2\pi D_m C_m f(D_m)}{A + B}(S - 1), \quad \text{(A21)}$$

where $S = q_v/q_{\text{sat}}$ is the saturation ratio, C_m is a particle shape factor, $f(D_p)$ is the so-called ''ventilation factor''

$$f(D_m) = a_{fm} + b_{fm} \text{Re}^{1/2} = a_{fm} + b_{fm} \left(\frac{\rho D_m v_m}{\mu}\right)^{1/2}. \quad \text{(A22)}$$

The coefficients A and B depend only on temperature and are written as

$$A = \frac{L}{K_a T}\left(\frac{L}{R_v T} - 1\right); \qquad B = \frac{R_v R}{D_a e_{\text{sat}}}, \quad \text{(A23)}$$

where $L = L_c$ for rain, $L = L_s$ for snow/graupel, and e_{sat} is the saturation water vapor pressure over water or ice. Integrating (A20), one can get the following expression for the rate of change of precipitating water type m mixing ratio due to evaporation:

$$\left(\frac{\partial q_m}{\partial t}\right)_{\text{evap}} = \frac{2\pi C_m N_{0m}}{\rho(A + B)} [A_{\text{em}} q_m^{1/2} + B_{\text{em}} q_m^{(5+b_m)/8}](S - 1), \quad \text{(A24)}$$

where

$$A_{\text{em}} = a_{\text{fm}} \left(\frac{\rho}{\pi \rho_m N_{0m}}\right)^{1/2}; \quad \text{(A25)}$$

$$B_{\text{em}} = b_{\text{fm}} \left(\frac{\rho a_m}{\mu}\right)^{1/2} \Gamma\left(\frac{5 + b_m}{2}\right) \left(\frac{\rho_o}{\rho}\right)^{0.25} \left(\frac{\rho}{\pi \rho_m N_{0m}}\right)^{(5+b_m)/8}. \quad \text{(A26)}$$

The rate of change of mass of a precipitating particle of type m due to collection of condensate of type l with mixing ratio q_l is assumed to follow the continuous growth equations as follows:

$$\left(\frac{\partial M_m}{\partial t}\right)_{\text{accr}} = \frac{\pi}{4} D_m^2 v_m E_{\text{ml}} \rho q_l, \quad \text{(A27)}$$

where E_{ml} is the collection efficiency factor. Integrating (A20), one can obtain the following expression for the rate of change of precipitating type m mixing ratio due to collection of condensate type l:

$$\left(\frac{\partial q_m}{\partial t}\right)_{\text{accr}} = A_{\text{am}} q_l q_m^{(3+b_m)/4}, \quad \text{(A28)}$$

where

$$A_{\text{am}} = \frac{\pi}{4} a_m N_{0m} E_{\text{ml}} \Gamma(3 + b_m) \left(\frac{\rho_o}{\rho}\right)^{0.5} \left(\frac{\rho}{\pi \rho_m N_{0m}}\right)^{(3+b_m)/4}. \quad \text{(A29)}$$

Note that, in the case ice is collected, A_{am} is multiplied by $\exp[0.025(T - 273.16)]$.

The source of precipitating water due to autoconversion of cloud water into rain is described following the original Kessler formulation:

$$\left(\frac{\partial q_p}{\partial t}\right)_{\text{auto}} = \max[0, \alpha(q_c - q_{co})], \quad \text{(A30)}$$

where α is the autoconversion rate coefficient, and q_{co} is a threshold liquid water mixing ratio. Aggregation of ice is parameterized similarly, except for the dependency on temperature (similar to Lin et al. 1983):

$$\left(\frac{\partial q_p}{\partial t}\right)_{\text{aggr}} = \max[0, \beta e^{0.025(T-273.16)}(q_i - q_{\text{io}})], \quad \text{(A31)}$$

where β is the aggregation rate coefficient, and $q_{\rm io}$ is a threshold ice amount.

Finally we note that, although we refer to the cloud ice as nonprecipitating water, it is actually allowed to fall with its own terminal velocity $V_{\rm TI}$. Sedimentation of ice affects q_T, and also changes h_L, since sedimentation itself does not change the air temperature. The corresponding tendencies are given by

$$\left(\frac{\partial q_T}{\partial t}\right)_{\rm sed} = \rho^{-1}\frac{\partial}{\partial z}\rho V_{TI} q_i, \quad \text{and} \tag{A32}$$

$$\left(\frac{\partial h_L}{\partial t}\right)_{\rm sed} = -(L_c + \omega_n L_f)\left(\frac{\partial q_T}{\partial t}\right)_{\rm sed}. \tag{A33}$$

The default set of the microphysics parameters is given in appendix B.

APPENDIX B
List of Constants

Symbol	Description	Value	Units
a_r	Constant in fall speed formula for rain	842*	$m^{1-b}\ s^{-1}$
a_s	Constant in fall speed formula for snow	4.84*	$m^{1-b}\ s^{-1}$
a_g	Constant in fall speed formula for graupel	94.5*	$m^{1-b}\ s^{-1}$
$a_{\rm fr}$	Constant in ventilation factor for rain	0.78**	
$a_{\rm fs}$	Constant in ventilation factor for snow	0.65**	
$a_{\rm fg}$	Constant in ventilation factor for graupel	0.78**	
b_r	Exponent in fall speed formula for rain	0.8*	
b_s	Exponent in fall speed formula for snow	0.25*	
b_g	Exponent in fall speed formula for graupel	0.5*	
$b_{\rm fr}$	Constant in ventilation factor for rain	0.31**	
$b_{\rm fs}$	Constant in ventilation factor for snow	0.44**	
$b_{\rm fg}$	Constant in ventilation factor for graupel	0.31**	
C_r	Rain shape factor	1.0**	
C_s	Snow shape factor	$2/\pi$**	
C_g	Graupel shape factor	1.0**	
C_p	Specific heat of air at constant pressure	1004	$J\ kg^{-1}\ K^{-1}$
D_a	Diffusion coefficient of water vapor at 0°C	2.210×10^{-5}	$m^2\ s^{-1}$
$E_{\rm rc}$	Collection efficiency of rain for cloud water	1.0*	
$E_{\rm sc}$	Collection efficiency of snow for cloud water	1.0*	
$E_{\rm gc}$	Collection efficiency of graupel for cloud water	1.0*	
$E_{\rm ri}$	Collection efficiency of rain for cloud ice	1.0*	
$E_{\rm si}$	Collection efficiency of snow for cloud ice	0.1**	
$E_{\rm gi}$	Collection efficiency of graupel for cloud ice	0.1*	
g	Gravitational acceleration	9.81	$m\ s^{-2}$
L_c	Latent heat of condensation	2.5104×10^6	$J\ kg^{-1}$
L_s	Latent heat of sublimation	2.8440×10^6	$J\ kg^{-1}$
L_f	Latent heat of fusion	0.3336×10^6	$J\ kg^{-1}$
N_{0r}	Intercept parameter for rain	8×10^{6}*	m^{-4}
N_{0s}	Intercept parameter for snow	3×10^{6}*	m^{-4}
N_{0g}	Intercept parameter for graupel	4×10^{6}**	m^{-4}
K_a	Thermal conductivity of air at 0°C	2.4×10^{-2}	$J\ m\ K^{-1}\ s^{-1}$
$q_{\rm co}$	Threshold cloud water for autoconversion	1×10^{-3}	$kg\ kg^{-1}$
$q_{\rm io}$	Threshold ice for aggregation	1×10^{-4}	$kg\ kg^{-1}$
R	Specific gas constant for air	287	$J\ kg^{-1}\ K^{-1}$
R_v	Specific gas constant for water vapor	461	$J\ kg^{-1}\ K^{-1}$
T_{0n}	Temperature threshold for ice	273.16	K
T_{0p}	Temperature threshold for snow/graupel	283.16	K
T_{0g}	Temperature threshold for graupel	283.16	K
T_{00n}	Temperature threshold for cloud water	253.16	K
T_{00p}	Temperature threshold for rain	268.16	K
T_{00g}	Temperature threshold for graupel	223.16	K
$V_{\rm TI}$	Terminal velocity for cloud ice	0.4	$m\ s^{-1}$
α	Autoconversion rate	0.001	s^{-1}
β	Ice aggregation rate	0.001	s^{-1}
ρ_o	Reference air density	1.29	$kg\ m^{-3}$
ρ_r	Density of rain	1000*	$kg\ m^{-3}$
ρ_s	Density of snow	100*	$kg\ m^{-3}$
ρ_g	Density of graupel	400**	$kg\ m^{-3}$
μ	Dynamic viscosity of air at 0°C	1.717×10^{-5}	$kg\ m^{-1}\ s^{-1}$

* As in Lin et al. (1983)
** As in Rutledge and Hobbs (1983, 1984)

REFERENCES

Betts, A. K., and M. J. Miller, 1986: A new convective adjustment scheme. Part II: Single column model tests using GATE wave, BOMEX, ATEX and arctic air-mass data sets. *Quart. J. Roy. Meteor. Soc.,* **112,** 693–709.

Bryan, G. H., and J. M. Fritsch, 2001: On adequate resolution for the simulation of deep moist convection: Theory and preliminary simulations. Preprints, *Ninth Conf. on Mesoscale Processes,* Fort Lauderdale, FL, Amer. Meteor. Soc., 288–292.

Deardorff, J. W., 1980: Stratocumulus-capped mixed layers derived from a three-dimensional model. *Bound.-Layer Meteor.,* **18,** 495–527.

Donner, L. J., C. J. Seman, and R. S. Hemler, 1999: Three-dimensional cloud system modeling of GATE convection. *J. Atmos. Sci.,* **56,** 1885–1912.

Ghan, S. J., and Coauthors, 2000: A comparison of single-column model simulations of summertime midlatitude continental convection. *J. Geophys. Res.,* **105** (D2), 2091–2124.

Grabowski, W. W., 1998: Toward cloud resolving modeling of large-scale tropical circulations: A simple cloud microphysics parameterization. *J. Atmos. Sci.,* **55,** 3283–3298.

——, X. Wu, M. W. Moncrieff, and W. D. Hall, 1998: Cloud-resolving modeling of cloud systems during Phase III of GATE. Part II: Effects of resolution and the third spatial dimension. *J. Atmos. Sci.,* **55,** 3264–3282.

——, ——, and ——, 1999: Cloud resolving modeling of tropical cloud systems during Phase III of GATE. Part III: Effects of cloud microphysics. *J. Atmos. Sci.,* **56,** 2384–2402.

Gregory, D., and M. J. Miller, 1989: A numerical study of the parameterization of deep tropical convection. *Quart. J. Roy. Meteor. Soc.,* **115,** 1209–1241.

Hack, J. J., and J. A. Pedretti, 2000: Assessment of solution uncertainties in single-column modeling frameworks. *J. Climate,* **13,** 352–365.

Khairoutdinov, M. F., and Y. L. Kogan, 1999: A large-eddy simulation model with explicit microphysics: Validation against aircraft observations of a stratocumulus-topped boundary layer. *J. Atmos. Sci.,* **56,** 2115–2131.

——, and D. A. Randall, 2001: A cloud resolving model as a cloud parameterization in the NCAR Community Climate System Model: Preliminary results. *Geophys. Res. Lett.,* **28,** 3617–3620.

Kiehl, J. T., J. J. Hack, G. B. Bonan, B. A. Boville, D. L. Williamson, and P. J. Rasch, 1998: The National Center for Atmospheric Research Community Climate Model: CCM3. *J. Climate,* **11,** 1131–1149.

Lin, Y.-L., R. D. Farley, and H. D. Orville, 1983: Bulk parameterization of the snow field in a cloud model. *J. Climate Appl. Meteor.,* **22,** 1065–1092.

Lord, S. J., H. E. Willoughby, and J. M. Piotrowicz, 1984: Role of a parameterized ice-phase microphysics in an axisymmetric, nonhydrostatic tropical cyclone model. *J. Atmos. Sci.,* **41,** 2836–2848.

Marshall, J. S., and W. McK. Palmer, 1948: The distribution of raindrops with size. *J. Meteor.,* **5,** 165–166.

Moeng, C.-H., and Coauthors, 1996: Simulation of a stratocumulus-topped planetary boundary layer: Intercomparison among different numerical codes. *Bull. Amer. Meteor. Soc.,* **77,** 261–278.

Petch, J. C., and M. E. B. Gray, 2001: Sensitivity studies using a cloud resolving model simulation of the tropical west Pacific. *Quart. J. Roy. Meteor. Soc.,* **127,** 2287–2306.

Randall, D. A., K.-M. Xu, R. J. C. Somerville, and S. Iacobellis, 1996: Single-column models and cloud ensemble model as links between observations and climate models. *J. Climate,* **9,** 1683–1697.

Redelsperger, J.-L., and Coauthors, 2000: A GCSS model intercomparison for a tropical squall line observed during TOGA-COARE. I: Cloud-resolving models. *Quart. J. Roy. Meteor. Soc.,* **126,** 823–864.

Rutledge, S. A., and P. V. Hobbs, 1983: The mesoscale and microscale structure and organization of clouds and precipitation in midlatitude cyclones. VIII: A model for the ''seeder-feeder'' process in warm-frontal rainbands. *J. Atmos. Sci.,* **40,** 1185–1206.

——, and ——, 1984: The mesoscale and microscale structure and organization of clouds and precipitation in midlatitude cyclones. XII: A diagnostic modeling study of precipitation development in narrow cold-front rainbands. *J. Atmos. Sci.,* **41,** 2949–2972.

Smolarkiewicz, P. K., and W. W. Grabowski, 1900: The multi-dimensional positive definite advection transport algorithm: Nonoscillatory option. *J. Comput. Phys.* **86,** 355–375.

Tao, W. K., and S.-T. Soong, 1986: A study of the response of deep tropical convection to mesoscale processes: Three-dimensional numerical experiments. *J. Atmos. Sci.,* **43,** 2653–2676.

——, J. Simpson, and S.-T. Soong, 1987: Statistical properties of a cloud ensemble: A numerical study. *J. Atmos. Sci.,* **44,** 3175–3187.

——, S. Lang, J. Simpson, W. S. Olson, D. Johnson, B. Ferrier, C. Kummerow, and R. Adler, 2000: Vertical profiles of latent heat release and their retrieval in TOGA COARE convective systems using a cloud resolving model, SSM/I and radar data. *J. Meteor. Soc. Japan,* **78,** 333–355.

Tompkins, A. M., 2000: The impact of dimensionality on long-term cloud resolving model simulations. *Mon. Wea. Rev.,* **128,** 1521–1535.

Weisman, M. L., W. C. Skamarock, and J. B. Klemp, 1997: The resolution dependence of explicitly modeled convective systems. *Mon. Wea. Rev.,* **125,** 527–548.

Xu, K.-M., and S. K. Krueger, 1991: Evaluation of cloudiness parameterization using cumulus ensemble model. *Mon. Wea. Rev.,* **119,** 342–367.

——, and D. A. Randall, 1995: Impact of interactive radiative transfer on the microscopic behavior of cumulus ensembles. Part I: Radiation parameterization and sensitivity test. *J. Atmos. Sci.,* **52,** 785–799.

——, and ——, 1996: Explicit simulation of cumulus ensembles with the GATE Phase III data: Comparison with observations. *J. Atmos. Sci.,* **53,** 3710–3736.

——, and Coauthors, 2002: An intercomparison of cloud-resolving models with the Atmospheric Radiation Measurement summer 1997 Intensive Observation Period data. *Quart. J. Roy. Meteor. Soc.,* **128,** 593–624.

Zhang, M.-H., J. L. Lin, R. T. Cederwall, J. J. Yio, and S. C. Xie, 2001: Objective analysis of ARM IOP data: Method, feature, and sensitivity. *Mon. Wea. Rev.,* **129,** 295–311.